Giant reversible magnetocaloric effect in the pyrochlore $Er_2Mn_2O_7$ due to a cooperative two-sublattice ferromagnetic order

Y. Q. Cai,[1,2] Y. Y. Jiao,[1,2] Q. Cui,[1,2] J. W. Cai,[3] Y. Li,[3] B. S. Wang,[1,2] M. T. Fernández-Díaz,[4] M. A. McGuire,[5] J.-Q. Yan,[5] J. A. Alonso,[6,*] and J.-G. Cheng[1,2,†]

[1]*Beijing National Laboratory for Condensed Matter Physics and Institute of Physics, Chinese Academy of Sciences, Beijing 100190, China*

[2]*University of Chinese Academy of Sciences, Beijing 100049, China*

[3]*College of Materials Science and Engineering, Beijing Institute of Petrochemical Technology, Beijing 102617, China*

[4]*Institut Laue Langevin, BP 156X, Grenoble, F-38042, France*

[5]*Materials Science and Technology Division, Oak Ridge National Laboratory, Oak Ridge, Tennessee 37831, USA*

[6]*Instituto de Ciencia de Materiales de Madrid, CSIC, Cantoblanco, E-28049 Madrid, Spain*

(Received 26 July 2017; revised manuscript received 16 October 2017; published 29 November 2017)

Most magnetic refrigeration materials showing a large and reversible magnetocaloric effect (MCE) undergo a second-order ferromagnetic (FM) transition involving large-moment magnetic species on one sublattice. A stronger MCE is expected near a cooperative FM order of two or more magnetic species with large magnetic moments residing on different sublattices, but experimental realizations are rare. Here we report on the discovery of large MCE in the cubic pyrochlore $Er_2Mn_2O_7$ near its second-order FM transition at $T_c \approx 34$ K; under the magnetic field change of 1 and 5 T, the maximum magnetic entropy change $-\Delta S_M$ is 5.27 and 16.1 J kg^{-1} K^{-1}, and the estimated magnetic refrigerant capacity reaches 68 and 522 J kg^{-1}, respectively. These latter values are among the largest for the known MCE materials. The observed giant and reversible MCE in $Er_2Mn_2O_7$ is mainly attributed to the large saturation moment of 18.9 μ_B per formula unit owing to a simultaneous FM ordering of the rear-earth Er^{3+} and transition-metal Mn^{4+} localized moments. Our results suggest that $Er_2Mn_2O_7$ pyrochlore is a promising candidate for magnetic refrigeration applications in the temperature range 20–80 K. More importantly, this work provides a new material system for developing high-performance MCE materials that can exhibit a strongly coupled FM transition involving two magnetic sublattices of large local moments in a single-phase material.

DOI: 10.1103/PhysRevMaterials.1.064408

I. INTRODUCTION

To develop energy efficient and environmentally benign technology is the main stream of advanced science and technology worldwide. Refrigeration based on the magnetocaloric effect (MCE) has attracted considerable attention in recent years because it consumes less energy and does not use greenhouse refrigerants [1]. In this field, much effort has been devoted to developing high performance magnetic refrigeration materials with a large MCE, that is, a large isothermal magnetic entropy change or a large adiabatic temperature change can be produced by the variation of magnetic field [2]. Since the discovery of giant MCE in Gd-Si-Ge [3,4], it became an important approach to explore magnetic refrigeration materials exhibiting a strongly first-order ferromagnetic (FM) transition. Several alloy systems including La-Fe-Si [5,6], Mn-Fe-P-As [7], Fe-Rh [8], Mn-Co-Ge [9], and Ni-Mn-X (X = Sn, In, Sb, Ga) based magnetic shape memory alloys [10–14] have been subsequently identified as giant MCE materials near room temperature (for a recent review see Ref. [15]). The efficiency of these materials decreases in fast cycling refrigeration due to thermal and magnetic hysteresis associated with the first-order transition [11]. In addition, the first-order nature might eventually lead to physical/chemical instability upon thermomagnetic cycling, which can drastically reduce the cooling efficiency [16]. Thus, a considerable amount of research has been undertaken to reduce the hysteresis losses via chemical substitutions or the insertion of interstitial atoms [9,13,17–19].

Alternatively, giant MCE materials associated with a *second-order* FM transition with fully reversible entropy changes are more suitable for practical applications [20]. In general, large and reversible MCE has been found in the rare-earth-based intermetallic compounds, such as binary *R*Ga [21–23], *RTr* [24], ternary *RTr*Al [25,26], *RTr*Si [27,28], and quaternary RNi_2B_2C [29–31], in which the large-moment rare-earth ions R = Gd, Tb, Dy, Ho, Er contribute to the large entropy change upon variation of magnetic field under isothermal conditions, while the transition metal ions Tr = Co, Ni, Fe, Cu are usually nonmagnetic and provide conduction electrons mediating the magnetic interactions between the R moments. In these cases, the magnetic degree of freedom for *Tr* is not utilized for the MCE. On the other hand, if both R and *Tr* sublattices can attain large localized moments and undergo a cooperative second-order FM transition, a stronger MCE might be achieved. In this regard, oxide materials are good candidates where both R and *Tr* can have well localized magnetic moments. However, the magnetic interactions between R and *Tr* moments are usually weak. Thus, R and *Tr* magnetic sublattices seldom order at the same temperature, with the ordering temperature for R usually significantly lower than that for *Tr*. For example, the $RTiO_3$ (R = Ho, Dy, Er) perovskites have been found to exhibit large MCE around the FM transition of Ti^{3+} ($S = 1/2$) sublattice [32–35]. But, in these cases the R moments are polarized gradually by the external magnetic field instead of participating in the FM order. As such, the

*ja.alonso@icmm.csic.es
†jgcheng@iphy.ac.cn

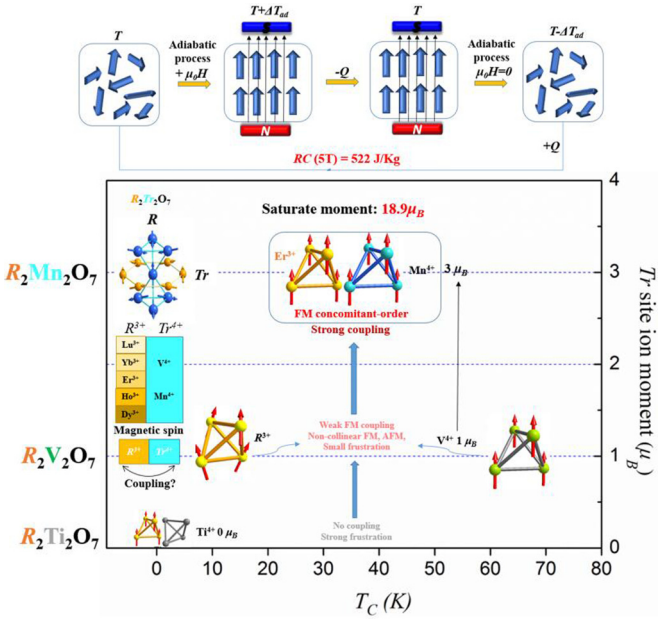

FIG. 1. Illustration of the magnetocaloric effect (top panel) and the magnetic coupling between R^{3+} and Tr^{4+} sublattices in the rare-earth transition-metal pyrochlores $R_2Tr_2O_7$ (Tr = Ti, V, Mn) (bottom panel).

MCE effect at low fields (e.g., $\mu_0 H < 2$ T) is usually small [32,33].

In this work we demonstrate that the cubic pyrochlores $R_2Mn_2O_7$ shows a large and reversible MCE at low fields owing to a unique "cooperative two-sublattice FM order." As shown in Fig. 1, the cubic pyrochlore of $R_2Tr_2O_7$ consists of three-dimensional interpenetrating network of corner-shared tetrahedra for both R and Tr sublattices [36]. As an archetype geometrically frustrated lattice, long-range antiferromagnetic order between localized R^{3+} moments is usually suppressed to below ~1 K in $R_2Ti_2O_7$ with nonmagnetic Ti^{4+} ($3d^0$, $S = 0$) [36,37]. In contrast, the geometrical frustration can be substantially relieved in $R_2V_2O_7$ [38], in which the magnetic V^{3+} ($3d^1$, $S = 1/2$) sublattice first undergoes a FM order below $T_c \sim 70$ K followed by the magnetic order of R^{3+} sublattice at lower temperatures; the form of the magnetic order of R^{3+} depends on the single-ion anisotropy. The coupling between R^{3+} and Tr^{4+} sublattices becomes stronger with enlarging the size of Tr^{4+} moment, and finally a simultaneous two-sublattice FM order is realized in $R_2Mn_2O_7$ with Mn^{4+} ($3d^3$, $S = 3/2$) below $T_c \sim 30-40$ K [36,39,40], leading to a huge saturation moment below T_c under a low magnetic field owing to a coalignment of the R^{3+} and Mn^{4+} moments. As we will show below, a large and reversible MCE is indeed achieved in $Er_2Mn_2O_7$ near its second-order FM transition at $T_c \approx 34$ K. Under the magnetic field change of 1 and 5 T, the estimated magnetic refrigerant capacity reaches 68 and 522 J kg^{-1}, respectively, larger than many well-known MCE materials including Gd [41] and $Gd_5Si_2Ge_2$ [17]. Our results not only demonstrate that $Er_2Mn_2O_7$ pyrochlore is a promising MCE material, but also provide a new platform for developing high-performance MCE materials consisting of two strongly FM coupled magnetic sublattices.

II. EXPERIMENTAL DETAILS

$R_2Tr_2O_7$ crystallizes in the cubic pyrochlore structure when the ionic radius ratio is in the range $1.46 \leqslant r_R/r_{Tr} \leqslant 1.80$ [42]. Because the cationic radius ratio $r_{Er}/r_{Mn} = 1.894$ falls out of the above range [43], $Er_2Mn_2O_7$ forms in the monoclinic layered perovskite structure when it is synthesized at ambient pressure [44]. In order to stabilize the cubic pyrochlore structure, polycrystalline $Er_2Mn_2O_7$ has to be synthesized under high pressure and high temperature conditions by incorporating an oxygen-releasing agent [42]. Fine powder of the starting precursor was first prepared via the wet-chemistry method by dissolving the mixture of Er_2O_3 and $MnCO_3$ in nitric acid [45]. Evaporation of the solution led to an organic resin, which was dried at 120 °C and decomposed at 600 °C for 12 h. The organic materials and the nitrates were eliminated in a subsequent treatment at 800 °C in air for 2 h. The resultant precursor powder was mixed with $KClO_4$ (30 wt. %), placed in a gold capsule, sealed and placed in a cylindrical graphite heater, and then subjected to heat treatment at 2 GPa at 1000 °C for 60 min. After releasing pressure, the resultant product was washed in water to dissolve KCl and then dried in air at 150 °C for 1 h. In order to obtain a dense $Er_2Mn_2O_7$ pellet, the phase pure powders were re-treated at 6 GPa and 1000 °C for 30 min by packing the powders in a gold capsule with separated $KClO_4$ pellets at both ends. All the subsequent measurements were performed on these pellet samples.

Phase purity of the obtained sample was examined with powder x-ray diffraction (XRD) at room temperature. For the structural refinement, neutron powder diffraction (NPD) experiments were carried out in the high-resolution powder diffractometer D2B ($\lambda = 1.594$ Å) at the Institut Laue Langevin in Grenoble. The patterns were collected at room temperature and 2 K. About 2 g of sample were contained in a vanadium cylinder; a time of 2 h was required to collect a full diffraction pattern. The NPD data were analyzed by the Rietveld method using the FULLPROF program. A pseudo-Voigt function was chosen to generate the line shape of the diffraction peaks. The following parameters were refined in the final run: scale factor, background coefficients, unit-cell parameters, zero-point error, and pseudo-Voigt profile parameters including asymmetry, positional coordinates, and isotropic thermal factors for all the atoms. The neutron scattering lengths for Er, Mn and O are 7.79, −3.75, and 5.80 fm, respectively. The magnetic properties were measured with a commercial Magnetic Property Measurement System (MPMS-III, Quantum Design). The specific heat was measured with the two-tau relaxation method in a Physical Property Measurement System (PPMS, Quantum Design).

III. RESULTS AND DISCUSSIONS

The XRD pattern (shown in Fig. S1 of the Supplemental Material [46]) confirms that the obtained $Er_2Mn_2O_7$ sample is single phase with the cubic pyrochlore structure. The lattice parameter $a = 9.8842(1)$ Å is consistent with the value reported previously [47]. To carry out a more accurate structural study of $Er_2Mn_2O_7$, we performed a NPD investigation at room temperature (RT) and 2 K. The NPD pattern at RT was fully refined in a cubic unit cell defined in the cubic Fd-3m

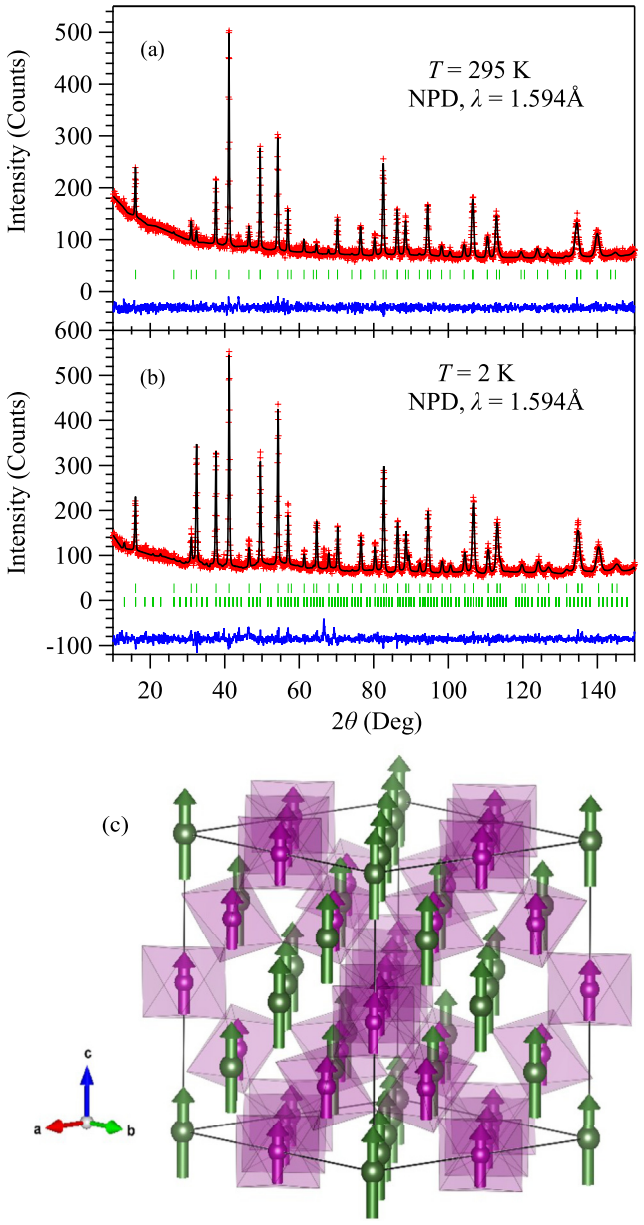

FIG. 2. Observed (crosses), calculated (solid line), and difference (at the bottom) NPD patterns of the $Er_2Mn_2O_7$ at (a) 295 K and (b) 2 K. The series of tick marks correspond to the positions of the allowed Bragg reflections for the main phase and the magnetic structure. (c) A schematic view of the magnetic structure, highlighting the spontaneous ferromagnetic coupling of Er^{3+} (green) and Mn^{4+} (purple) magnetic moments.

space group with origin at (1/8,1/8,1/8). In this setting the Er cations are located at 16*c* (0,0,0) sites, the Mn cations are placed at 16*d* (1/2,1/2,1/2) positions, and the two kinds of nonequivalent oxygen atoms (O1 and O2) at 48*f* (*x*,1/8,1/8) and 8*b* (1/8,1/8,1/8) sites, respectively. Figure 2(a) illustrates the good agreement between the observed and calculated NPD patterns at RT. Table I summarizes the main results after the Rietveld refinements, including the unit cell, atomic and thermal parameters, main interatomic distances and angles, and the discrepancy factors.

TABLE I. Unit cell, positional, thermal parameters, ordered magnetic moments, selected bond lengths, and angles for $Er_2Mn_2O_7$ in cubic *Fd*-3*m* (No. 227) space group from NPD data at 295 and 2 K. Er atoms are placed at 16*c* (0,0,0), Mn at 16*d* (1/2,1/2,1/2), O1 at 48*f* (*x*,1/8,1/8), O2 at 8*b* (1/8,1/8,1/8) Wyckoff sites.

Temperature (K)	295	2
a (Å)	9.8921(4)	9.8806(2)
V (Å^3)	967.96(6)	964.61(4)
Er		
B (Å^2)	0.36(11)	0.00(8)
Mn		
B (Å^2)	0.94(14)	0.56(11)
O1		
x	0.4210(2)	0.4206(2)
B (Å^2)	0.53(9)	0.29(8)
O2		
B (Å^2)	0.2(2)	0.0(1)
Magn. mom. Mn (μ_B)	–	2.92(8)
Magn. mom. Er (μ_B)	–	4.26(11)
Bond lengths (Å)		
Er-O1(×6)	2.4430(11)	2.4274(14)
Er-O2(×2)	2.14170(5)	2.13921(3)
Mn-O1(×6)	1.9154(11)	1.9148(11)
Bond angles (deg)		
Er-O1-Er	91.90(5)	92.04(4)
Er-O2-Er	109.47	109.47
Mn-O1-Mn	131.84(3)	131.63(3)
Reliability factors		
χ^2	1.12	1.11
R_p (%)	4.16	4.89
R_{wp} (%)	5.30	6.17
R_{expt} (%)	5.36	5.86
R_{mag} (%)	–	9.02
R_I (%)	3.32	4.95

The NPD pattern collected at $T = 2$ K contains additional scattering of magnetic origin. As illustrated in Fig. S2 [46], the intensities of low-angle reflections, typically (222), (400), (511), (440), and (531), increase considerably in comparison with those at 295 K, which is attributed to the establishment of a long-range magnetically ordered structure. As the size of the magnetic and crystallographic unit cell is coincident, the propagation vector is $\mathbf{k} = 0$. A satisfactory solution was found by modeling *a collinear FM coupling between Mn and the Er magnetic sublattices*. Figure 2(b) illustrates the Rietveld refinement of the NPD pattern at 2 K; the second series of Bragg reflections corresponds to the magnetic reflections. The refined magnetic moments were considered to be oriented along the [001] axis since it is impossible to determine their orientations in a cubic system. This arrangement defines a perfectly collinear ferromagnetic structure, as shown in Fig. 2(c). The ordered magnetic moments determined at 2 K are 2.92(8) μ_B for Mn cations and 4.26(11) μ_B for Er cations. The former is close to that expected for $Mn^{4+}(t_{2g}{}^3)$, indicating a full long-range magnetic ordering at 2 K. In contrast, the ordered moment of the Er^{3+} is smaller than that determined by neutron diffraction in other Er-containing oxides, for instance 7.89 μ_B in Er_2BaNiO_5 [48].

We can understand the collinear FM order and the reduced Er^{3+} moment in light of the local structures. The spontaneous FM order of the Mn sublattice should be ascribed to the virtual charge transfer between the filled t_{2g} and the empty e_g orbitals of Mn^{4+} due to the strong bending of Mn-O-Mn angle of ~130° (see Table I). The strong internal magnetic field generated by the ferromagnetically ordered Mn^{4+} ($S = 3/2$) sublattice can align the large Er^{3+} moment via the dipolar interactions. However, a full alignment of Er^{3+} moment is hindered by the considerable single-ion anisotropy as a result of the spin-orbit coupling and the local site distortion featured by the six long Er-O1 and two short Er-O2 bonds (Table I). For example, a strong *XY* anisotropy with the moment lying with the plane perpendicular to the local ⟨111⟩ axis has been well characterized in the similar $Er_2Tr_2O_7$ (Tr = Ti, Ge, Pt) pyrochlores, in which the Er^{3+} moment saturates to ~4.5 μ_B under 5 T [49,50]. This value corresponds to the observed Er^{3+} moment at zero field in $Er_2Mn_2O_7$. Then, a moderate external field is able to fully polarize the Er^{3+} moments, as shown in Fig. 3(b) below.

The collinear two-sublattice FM order of $Er_2Mn_2O_7$ was also confirmed by measurements of bulk magnetic properties. The main panel of Fig. 3(a) displays the temperature dependence of the magnetic susceptibility $\chi(T)$ measured under an external field of $\mu_0 H = 0.1$ T by three procedures: the ZFCw and FCw curves were recorded upon warming up after zero-field cooled (ZFC) and field cooled (FC) from room temperature, respectively, while FCc data were recorded upon cooling down from room temperature under magnetic field. The sharp increase of $\chi(T)$ corresponds to the paramagnetic to FM transition at $T_c = 34.5$ K, which can be defined as the peak position of $d\chi/dT$ and agrees well with the reported value in literature [36]. A slight splitting of ZFC and FC curves below 15 K could be caused by the magnetocrystalline anisotropy or magnetic domains. No thermal hysteresis was observed between the FCw and FCc curves, in accordance with the second-order nature of the transition. A detailed analysis based on the Arrott plots and the Banerjee criterion further confirms that the FM transition in $Er_2Mn_2O_7$ is of second-order type (see Fig. S3) [51].

The inverse magnetic susceptibility $\chi^{-1}(T)$ shown in the inset of Fig. 3(a) follows nicely the Curie-Weiss (CW) behavior in the paramagnetic region; a CW fitting to $\chi^{-1}(T)$ in the temperature range 50–300 K yields an effective moment of $\mu_{\text{eff}} = 10.46\,\mu_B$ per ($ErMnO_{3.5}$) and a CW temperature $\theta_{\text{CW}} = +37.4$ K. The obtained μ_{eff} agrees well with the theoretical value of $\mu_{\text{eff}}^{\text{theo}} = \{[\mu_{\text{eff}}(Er^{3+})]^2 + [\mu_{\text{eff}}(Mn^{4+})]^2\}^{1/2} = 10.34\,\mu_B$ for both localized Er^{3+} and Mn^{4+} moments, and the positive θ_{CW} signals a dominant FM interaction between the magnetic moments. As such, the geometrical frustration is completely relieved, giving rise to a $\theta_{\text{CW}}/T_c \approx 1$. Since the sister compounds $(Y/Lu)_2Mn_2O_7$ with nonmagnetic Y^{3+} or Lu^{3+} ions exhibit a lower $T_c \approx 15-20$ K for the FM order of Mn^{4+} sublattice [40], the higher T_c of $Er_2Mn_2O_7$ should be attributed to the cooperative couplings between Er^{3+} and Mn^{4+} moments.

Figure 3(b) depicts the isothermal magnetization $M(\mu_0 H)$ of $Er_2Mn_2O_7$ measured at 2 K between −7 and +7 T. A typical FM behavior is observed and the saturation moment reaches a large value of 18.9 μ_B/f.u. (189.6 emu/g), which can account for ~80% of the ideal value of 24 μ_B for a full FM alignment

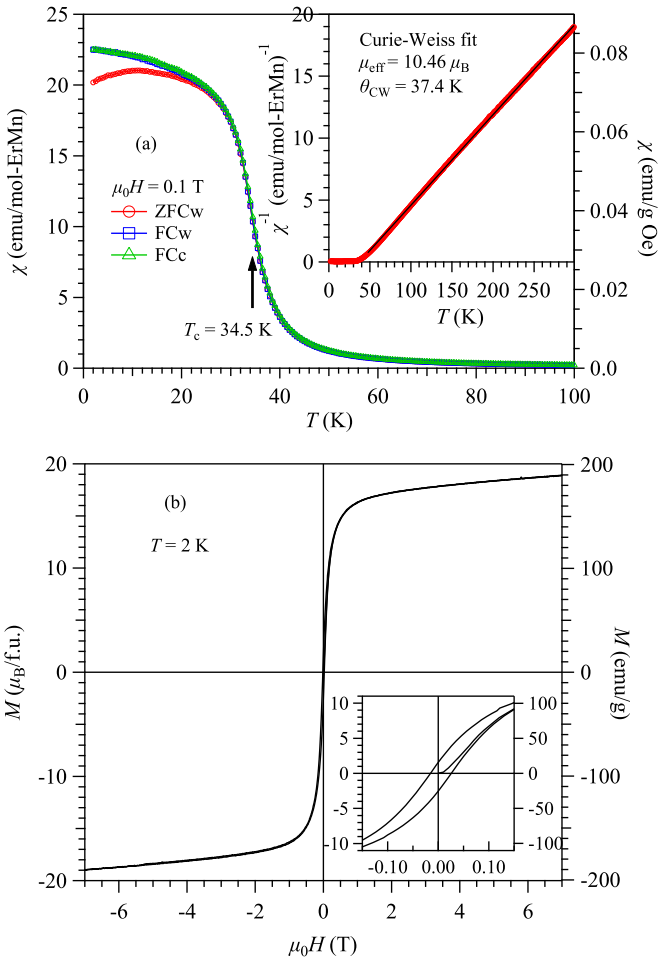

FIG. 3. (a) Temperature dependence of the dc magnetic susceptibility $\chi(T)$ for $Er_2Mn_2O_7$ measured under $\mu_0 H = 0.1$ T at different procedures: ZFCw and FCw recorded upon warming up after zero-field cooled and field cooled from room temperature, FCc recorded during cooling down under field. The $T_c = 34.5$ K was determined from the minimum of $d\chi/dT$. Inset shows the inverse $\chi^{-1}(T)$ fitted with Curie-Weiss law. (b) The isothermal magnetization loop $M(\mu_0 H)$ at 2 K. Inset shows an enlarged view of the $M(\mu_0 H)$ curve near the origin.

of Er^{3+} (9 μ_B) and Mn^{4+} (3 μ_B). Such a discrepancy should be attributed to the magnetic domains or defects due to the polycrystalline nature. As seen in the inset of Fig. 3(b), a small coercive force $\mu_0 H_c \approx 0.02$ T for $M(\mu_0 H)$ at 2 K signals a weak magnetic hysteresis.

The presence of second-order FM transition with a large saturation moment in the cubic pyrochlore $Er_2Mn_2O_7$ motivated us to evaluate its MCE, which had *never* been studied before to the best of our knowledge. First, we measured a series of isothermal magnetization curves $M(\mu_0 H)$ between 2 and 100 K as shown in Fig. 4(a). Then, we calculated the magnetic entropy change ΔS_M according to the Maxwell relation:

$$\Delta S_M\left(\frac{T_1+T_2}{2}\right) = \frac{1}{T_1-T_2}\left[\int_0^{\mu_0 H} M(T_2,\mu_0 H)d(\mu_0 H) - \int_0^{\mu_0 H} M(T_1,\mu_0 H)d(\mu_0 H)\right]. \quad (1)$$

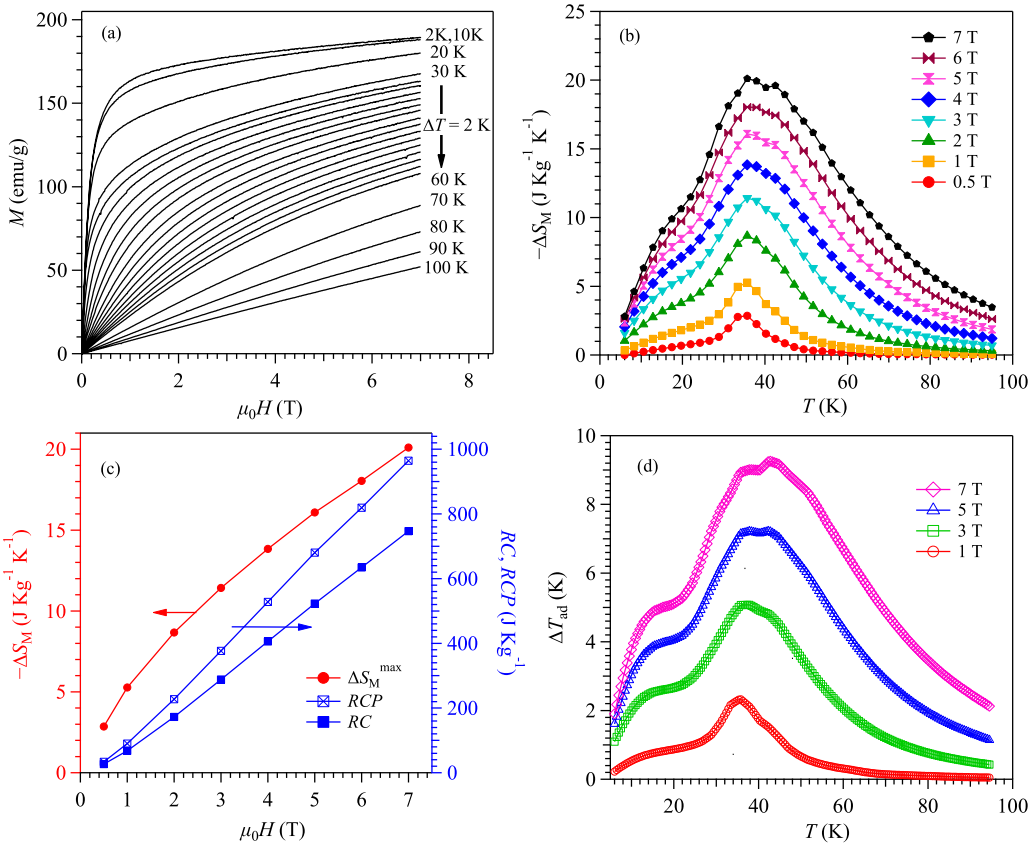

FIG. 4. (a) Isothermal magnetization $M(\mu_0 H)$ curves from 2 to 100 K. (b) Temperature dependence of the magnetic entropy change $-\Delta S_M$ under different field changes up to 7 T. (c) Field dependences of the maximum $-\Delta S_M$, the refrigerant capacity (*RC*), and the relative cooling power (*RCP*). (d) Temperature dependence of the adiabatic temperature change ΔT_{ad} under different magnetic fields.

The obtained $-\Delta S_M$ as a function of temperature under various magnetic fields are displayed in Fig. 4(b). As can be seen, the $-\Delta S_M(T)$ curves cover a relatively broad temperature range centered on T_c, which moves slightly to higher temperatures with increasing magnetic field. The maximum values of $-\Delta S_M$ reach 2.86, 5.3, 8.7, 11.4, 13.8, 16.1, 18.0, and 20.1 J kg^{-1} K^{-1} under a field change of 0.5, 1, 2, 3, 4, 5, 6, and 7 T, respectively, as shown in Fig. 4(c). The $-\Delta S_M$ values at high magnetic fields are comparable to those observed in $TbMnO_3$ and $HoMnO_3$ single crystals along the easy axis, but the values at low fields under 1 T are significantly higher than those of $TbMnO_3$ and $HoMnO_3$ [52,53]. As will be discussed below, the superior performance at low field for $Er_2Mn_2O_7$ should be attributed to the spontaneous order of Er^{3+} moments rather than the gradual polarization by an external magnetic field as in $TbMnO_3$ and $HoMnO_3$ [53]. The field dependence of maximum ΔS_M was plotted in Fig. S4 in the form of $-\Delta S_M$ versus $(\mu_0 H)^{2/3}$, and the observed excellent linear behavior is consistent with the expectation for an FM transition as derived by Oesterreicher and Parker [54].

In addition to a large ΔS_M, a potential magnetic refrigerant material should also attain a large refrigerant capacity (*RC*), which represents the amount of heat that can be transferred between the cold and hot sinks in one thermodynamic cycle. In practice, *RC* can be calculated via [55]

$$RC = \int_{T_{cold}}^{T_{hot}} \Delta S_M dT, \tag{2}$$

where T_{cold} and T_{hot} represent the corresponding temperatures at the full width at the half maximum (FWHM) of the $-\Delta S_M(T)$ peak [14,17]. Thus, a broad $-\Delta S_M(T)$ curve gives a larger *RC*. Although the maximum $|\Delta S_M|$ values are not very high among known MCE materials, the relatively broad $-\Delta S_M(T)$ curves in Fig. 4(b) should offer a very competitive *RC*. Then, we determined the *RC* under each field change by integrating the corresponding $-\Delta S_M(T)$ curve within the FWHM region, as illustrated in Figs. S5(a)–S5(d) for 1, 3, 5, and 7 T. On the other hand, we also estimated the relative cooling power $RCP = -\Delta S_M{}^{max} \delta T_{FWHM}$, which is roughly 4/3 times of the *RC* value based on a simple geometrical consideration [1].

The obtained *RC* and *RCP* values as a function of magnetic field are plotted in Fig. 4(c). As can be seen, both *RC* and *RCP* of $Er_2Mn_2O_7$ increase almost linearly with magnetic field, and *RC* (*RCP*) values reach 68 (90), 288 (377), 522 (680), and 747 (964) J kg^{-1} under a field change of 1, 3, 5, and 7 T, respectively. The *RC* of $Er_2Mn_2O_7$ under a field change

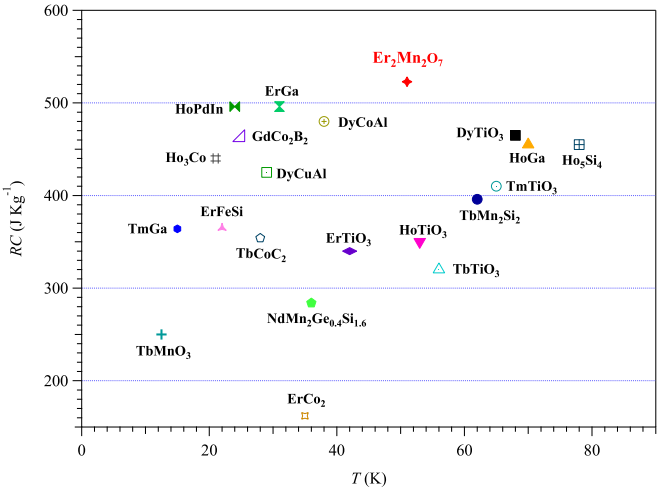

FIG. 5. *RC* values of $Er_2Mn_2O_7$ and other MCE materials in the similar temperature range: $NdMn_2Ge_{0.4}Si_{1.6}$ [62], $GdCo_2B_2$ [63], $TbMnO_3$ [52], $TbMn_2Si_2$ [64], $TbFeO_3$ [65], $TbCoC_2$ [66], $DyTiO_3$ [34], DyCoAl [26], DyCuAl [25], $HoTiO_3$ [32], HoGa [23], HoPdIn [67], Ho_3Co [68], Ho_5Si_4 [69], $ErTiO_3$ [33], ErFeSi [27], ErGa [21], $ErCo_2$ [70], TmGa [71], and $TmTiO_3$ [35].

of 5 T is compared in Fig. 5 with the most studied MCE materials in the similar temperature range. It can be seen that the *RC* value of $Er_2Mn_2O_7$ is quite large, and almost twice that of $ErTiO_3$ (340 J kg^{-1}) [33] and $TbMnO_3$ (250 J kg^{-1}) [52] single crystals with similar rare-earth moment. Such a giant *RC* makes $Er_2Mn_2O_7$ a very promising MCE material in the temperature range 20−80 K.

To make a comprehensive characterization, we also evaluated the adiabatic temperature change ΔT_{ad} by measuring specific heat under zero field. As shown in Fig. S6(a), the specific heat of $Er_2Mn_2O_7$ displays a λ-shaped anomaly peaked at $T_c = 32.6$ K, corresponding to the second-order FM transition. ΔT_{ad} was calculated according to the equation $\Delta T_{ad} = -\Delta S_M(T,\mu_0 H)T/C_p(T,\mu_0 H_0)$, where $C_p(T, \mu_0 H_0)$ is the zero-field specific heat. Since the specific-heat peak at T_c is usually smeared out under magnetic fields, we have performed a polynomial fitting to $C_p(T, 0\ \mathrm{T})$ by leaving out the data near T_c, as shown by the C_{fit} in Fig. S6(a).

The obtained $\Delta T_{ad} \approx -\Delta S_M(T,\mu_0 H)T/C_{fit}$ as a function of temperature under 1, 3, 5, and 7 T are displayed in Fig. 4(d). Under a magnetic field change of 5 T, the ΔT_{ad} of $Er_2Mn_2O_7$ can reach ∼7 K, which is comparable with the most MCE materials with a second-order phase transition, such as ErFeSi (5.7 K) [27], $TbMnO_3$ (7.5 K) [53], and DyCuAl (7.7 K) [25].

These above characterizations confirm that $Er_2Mn_2O_7$ can be regarded as a new magnetic refrigeration material with a large and reversible MCE in a relatively broad temperature near its FM transition. In comparison with the known MCE materials in the similar temperature range, the observed maximum magnetic entropy change $-\Delta S_M$ (e.g., 16.1 J kg^{-1} K^{-1} at 5 T) and the adiabatic temperature change ΔT_{ad} (e.g., ∼7 K at 5 T) are not particularly large considering the huge saturation moment of 18.9 μ_B/f.u (189.6 emu/g) for $Er_2Mn_2O_7$. This is presumably caused by the smooth variation of $M(T)$ near T_c since both ΔS_M and ΔT_{ad} are proportional to the temperature derivative of magnetization dM/dT [1]. As we know, the sharpness of the transition depends sensitively on the degree of crystallization, magnetic anisotropy, and/or defects; high-quality single crystalline samples with the magnetic field applied along the easy axis are beneficial for a better MCE performance [52]. In the present case, the polycrystalline sample with randomly oriented magnetic domains was studied; we expect to achieve higher $-\Delta S_M$ and ΔT_{ad} if a better quality or a single crystalline sample can be measured.

While the observed $-\Delta S_M$ and ΔT_{ad} are not optimized, $Er_2Mn_2O_7$ exhibits an exceptionally high refrigerant capacity *RC*, e.g., 522 J kg^{-1} at 5 T, as illustrated in Fig. 5. This is mainly attributed to the broad $-\Delta S_M(T)$ curves in Fig. 4(b). The large *RC* implies that $Er_2Mn_2O_7$ has a wide working temperature range. Then, a reasonable $\Delta T_{ad} \sim 7$ K with a large *RC* can still make $Er_2Mn_2O_7$ quite appealing in real refrigeration applications.

Another noteworthy advantage of $Er_2Mn_2O_7$ is the low-field MCE applications suitable for the permanent magnets. Under a low magnetic field change of 1 T, $Er_2Mn_2O_7$ can still exhibit a considerable large $-\Delta S_M = 5.3$ J kg^{-1} K^{-1} and $RC = 68$ J kg^{-1}. These values at such low fields become negligibly small for many oxide MCE materials such as $TbMnO_3$ [52,53]. Such an excellent low-field performance should be attributed to the cooperative FM ordering of the Er^{3+} and Mn^{4+} moments at T_c so that the magnetic response at low fields is strong. In contrast, the large rare-earth moment in $TbMnO_3$ has to be polarized by a high magnetic field since the coupling between Tb^{3+} and Mn^{3+} is very weak in the perovskite structure [53].

Therefore, our present study demonstrated that the pyrochlore $Er_2Mn_2O_7$ is a promising MCE material in the temperature range 20–80 K. Its high performance should be largely attributed to the cooperative FM order of the Er^{3+} and Mn^{4+}, two large-moment sublattices. Since the MCE depends mainly on the magnitude of the magnetic moments and its temperature dependence at T_c, such a cooperative two-lattice FM co-order that can produce a larger magnetic moment provides a new approach for designing high-performance MCE materials. The $RTiO_3$ (R = Gd, Tb, . . . , Lu) perovskites are rare examples that can form FM order for the Ti^{3+} sublattice [56], and the involvement of orbital order at the FM transition can produce a large entropy change comparable to that of $Er_2Mn_2O_7$. However, the R^{3+} sublattice in $RTiO_3$ does not participate in the FM order, leading to a smaller *RC* and weak low-field performance [33]. In a similar way, the contribution from the rare-earth sublattice is also insignificant in the perovskite manganites that have also been considered as good MCE materials [57,58].

In comparison with the perovskites, the magnetic coupling between the R^{3+} and Tr^{4+} sublattices that form a buckled hexagon can be substantially enhanced in the $R_2Tr_2O_7$ pyrochlores as illustrated in the inset of Fig. 1, and the magnetic interactions should be proportional to their moment sizes. $R_2Mn_2O_7$ is probably the system hosting the largest *Tr*-site magnetic moment among the 3*d* transition-metal-based pyrochlore systems since the $R_2Tr_2O_7$ (Tr = Fe, Co, Ni)

cannot be stabilized in the pyrochlore structure. When the *Tr* is occupied by a 4*d*- or 5d-transition metal ion [59,60], its moments is usually small, and their couplings to R^{3+} are weak. Thus, $R_2Mn_2O_7$ is likely the best candidate system among the pyrochlore oxides that are suitable for MCE applications considering the cooperative FM ordering of the large magnetic moments on both sites. The performance can be further optimized via improving the sample quality, making the FM transition sharper, or replacing Er^{3+} with larger-moment ions such as Ho^{3+} or Dy^{3+}. Moreover, such a "cooperative two-sublattice FM order" can also be explored in other structural families of compounds.

The importance of two-sublattice FM order in the cubic pyrochlore structure for the giant MCE is further elaborated by a comparison with the isomeric "$Er_2Mn_2O_7$" synthesized at ambient pressure [44,61]. It crystallizes in a monoclinic layered perovskite structure (space group $P2/m$), and undergoes an antiferromagnetic transition at a rather low $T_N \approx 2$ K. For this monoclinic phase, the magnetization $M(\mu_0 H)$ curves at low temperatures exhibit a weak ferromagneticlike behavior, but the saturation moment is only $7.66\,\mu_B$/f.u. In addition, the MCE can only be observed at low temperatures around T_N with a small $-\Delta S_M = 2.35\,\mathrm{J\,kg^{-1}\,K^{-1}}$ under a field change of 5 T [61]. Both the saturation moment and the $-\Delta S_M$ for the monoclinic phase are much lower than those observed in the cubic pyrochlore phase in the present work. These comparisons thus demonstrate that the two-sublattice cooperative FM order that produces a large saturation moment is essential for the giant MCE in the cubic pyrochlore $Er_2Mn_2O_7$.

IV. CONCLUSION

In summary, we demonstrated that the cubic pyrochlore $Er_2Mn_2O_7$ exhibits a large and reversible MCE near its second-order FM transition, showing a considerable large magnetic entropy change $-\Delta S_M$ of $16.1\,\mathrm{J\,kg^{-1}\,K^{-1}}$ and a giant magnetic refrigerant capacity RC of $522\ \mathrm{J\,kg^{-1}}$ under a magnetic field change of 5 T. In particular, its low-field performances of $-\Delta S_M = 5.3\,\mathrm{J\,kg^{-1}\,K^{-1}}$ and $RC = 68\,\mathrm{J\,kg^{-1}}$ are quite compelling for practical applications. The observed giant and reversible MCE in $Er_2Mn_2O_7$ is largely attributed to simultaneous two-sublattice FM order of the Er^{3+} and Mn^{4+} localized moments, acquiring a huge saturation moment of $18.9\,\mu_B$/f.u. Our results thus demonstrate $R_2Mn_2O_7$ pyrochlore as a promising new platform for high-performance MCE materials.

ACKNOWLEDGMENTS

We thank Dr. J.-S. Zhou for useful discussions. Y.Q.C. acknowledges the UCAS Joint PhD Training Program. J.-G.C. is supported by the CAS, NSFC, and MOST of China (Grants No. QYZDBSSW-SLH013, No. 11574377, No. XDB07020100, and No. 2014CB921500). Y.L. is supported by the NSFC (Grant No. 51402019) and the Beijing Natural Science Foundation (Grant No. 2152011). M.A.M. and J.-Q.Y. are supported by the U.S. Department of Energy, Office of Science, Basic Energy Sciences, Materials Sciences and Engineering Division. J.A.A. grateful acknowledges the Spanish MINECO for granting the project MAT2013-41099-R.

Y.Q.C., Y.Y.J., and Q.C. contributed equally to this work.

[1] K. A. Gschneidner Jr. and V. K. Pecharsky, Annu. Rev. Mater. Sci. **30**, 387 (2000).
[2] K. A. Gschneidner Jr., V. K. Pecharsky, and A. O. Tsokol, Rep. Prog. Phys. **68**, 1479 (2005).
[3] V. K. Pecharsky and K. A. Gschneidner Jr., Phys. Rev. Lett. **78**, 4494 (1997).
[4] V. K. Pecharsky and K. A. Gschneidner Jr., Appl. Phys. Lett. **70**, 3299 (1997).
[5] F. X. Hu, B. G. Shen, J. R. Sun, Z. H. Cheng, G. H. Rao, and X. X. Zhang, Appl. Phys. Lett. **78**, 3675 (2001).
[6] F. X. Hu, B. G. Shen, J. R. Sun, and Z. H. Cheng, Phys. Rev. B **64**, 012409 (2001).
[7] O. Tegus, E. Bruck, K. H. J. Buschow, and F. R. de Boer, Nature (London) **415**, 150 (2002).
[8] E. Stern-Taulats, A. Gràcia-Condal, A. Planes, P. Lloveras, M. Barrio, J.-L. Tamarit, S. Pramanick, S. Majumdar, and L. Mañosa, Appl. Phys. Lett. **107**, 152409 (2015).
[9] N. T. Trung, L. Zhang, L. Caron, K. H. J. Buschow, and E. Bruck, Appl. Phys. Lett. **96**, 172504 (2010).
[10] T. Krenke, E. Duman, M. Acet, E. F. Wassermann, X. Moya, L. Manosa, and A. Planes, Nat. Mater. **4**, 450 (2005).
[11] J. Liu, T. Gottschall, K. P. Skokov, J. D. Moore, and O. Gutfleisch, Nat. Mater. **11**, 620 (2012).
[12] S. Stadler, M. Khan, J. Mitchell, N. Ali, A. M. Gomes, I. Dubenko, A. Y. Takeuchi, and A. P. Guimaraes, Appl. Phys. Lett. **88**, 192511 (2006).
[13] E. Stern-Taulats *et al.*, Acta Mater. **96**, 324 (2015).
[14] L. Huang, Y. H. Qu, D. Y. Cong, X. M. Sun, and Y. D. Wang, Shap. Mem. Superelasticity **3**, 218 (2017).
[15] X. Moya, S. Kar-Narayan, and N. D. Mathur, Nat. Mater. **13**, 439 (2014).
[16] J. Torrens-Serra, C. A. Biffi, R. Santamarta, V. Recarte, J. I. Perez-Landazabal, A. Tuissi, and E. Cesari, Mater. Charact. **93**, 24 (2014).
[17] V. Provenzano, A. J. Shapiro, and R. D. Shull, Nature (London) **429**, 853 (2004).
[18] B. Gao, F. X. Hu, J. Wang, J. Shen, J. R. Sun, and B. G. Shen, J. Appl. Phys. **105**, 07A916 (2009).
[19] H. Zhang, B. G. Shen, Z. Y. Yu, X. Q. Zheng, J. Shen, F. X. Hu, J. R. Sun, and Y. Long, J. Appl. Phys. **111**, 07A909 (2012).
[20] S. Singh *et al.*, Adv. Mater. **28**, 3321 (2016).
[21] J. Chen, B. G. Shen, Q. Y. Dong, F. X. Hu, and J. R. Sun, Appl. Phys. Lett. **95**, 132504 (2009).
[22] X. Q. Zheng *et al.*, J. Appl. Phys. **111**, 07A917 (2012).
[23] J. Chen, B. G. Shen, Q. Y. Dong, and J. R. Sun, Solid State Commun. **150**, 157 (2010).
[24] L. W. Li, Y. Yuan, Y. K. Zhang, R. Pöttgen, and S. Q. Zhou, J. Alloy. Comp. **643**, 147 (2015).
[25] Q. Y. Dong, B. G. Shen, J. Chen, J. Shen, and J. R. Sun, J. Appl. Phys. **105**, 113902 (2009).
[26] X. X. Zhang, F. W. Wang, and G. H. Wen, J. Phys.: Condens. Matter **13**, L747 (2001).

[27] H. Zhang, B. G. Shen, Z. Y. Xu, J. Shen, F. X. Hu, J. R. Sun, and Y. Long, Appl. Phys. Lett. **102**, 092401 (2013).
[28] H. Zhang, Y. J. Sun, E. Niu, L. H. Yang, J. Shen, F. X. Hu, J. R. Sun, and B. G. Shen, Appl. Phys. Lett. **103**, 202412 (2013).
[29] L. W. Li and K. Nishimura, Appl. Phys. Lett. **95**, 132505 (2009).
[30] L. W. Li, M. Kadonaga, D. X. Huo, Z. H. Qian, T. Namiki, and K. Nishimura, Appl. Phys. Lett. **101**, 122401 (2012).
[31] L. W. Li, K. Nishimura, M. Kadonaga, Z. H. Qian, and D. X. Huo, J. Appl. Phys. **110**, 043912 (2011).
[32] Y. T. Su, Y. Sui, J.-G. Cheng, X. J. Wang, Y. Wang, W. F. Liu, and X. Y. Liu, J. Appl. Phys. **110**, 083912 (2011).
[33] Y. Su, Y. Sui, J.-G. Cheng, J.-S. Zhou, X. Wang, Y. Wang, and J. B. Goodenough, Phys. Rev. B **87**, 195102 (2013).
[34] Y. T. Su, Y. Sui, X. J. Wang, J.-G. Cheng, Y. Wang, W. F. Liu, and X. Y. Liu, Mater. Lett. **72**, 15 (2012).
[35] Y. T. Su, Y. Sui, J.-G. Cheng, X. J. Wang, Y. Wang, P. Liu, and J. K. Tang, J. Appl. Phys. **111**, 07A925 (2012).
[36] J. S. Gardner, M. J. P. Gingras, and J. E. Greedan, Rev. Mod. Phys. **82**, 53 (2010).
[37] J. A. Hodges *et al.*, Phys. Rev. Lett. **88**, 077204 (2002).
[38] Z. L. Dun *et al.*, Phys. Rev. B **91**, 064425 (2015).
[39] J. E. Greedan, N. P. Raju, A. Maignan, C. Simon, J. S. Pedersen, A. M. Niraimathi, E. Gmelin, and M. A. Subramanian, Phys. Rev. B **54**, 7189 (1996).
[40] N. Imamura, M. Karppinen, H. Yamauchi, and J. B. Goodenough, Phys. Rev. B **82**, 132407 (2010).
[41] G. V. Brown, J. Appl. Phys. **47**, 3673 (1976).
[42] M. A. Subramanian, G. Aravamudan, and G. V. Subba Rao, Prog. Solid State Chem. **15**, 55 (1983).
[43] R. D. Shannon, Acta Crystallogr. Sect. A **32**, 751 (1976).
[44] N. Ben Amor, M. Bejar, E. Dhahri, M. A. Valente, P. Lachkar, and E. K. Hlil, J. Rare Earth **31**, 54 (2013).
[45] S. Brown, H. C. Gupta, J. A. Alonso, and M. J. Martinez-Lope, J. Raman Spectrosc. **34**, 240 (2003).
[46] See Supplemental Material at http://link.aps.org/supplemental/10.1103/PhysRevMaterials.1.064408 the XRD pattern at room temperature, the NPD patterns at RT and 2 K, the Arrott plot, the specific heat at zero field, and the detials for the calculation of refrigerant capacity and the adiabatic temperature change.
[47] M. A. Subramanian, C. C. Torardi, D. C. Johnson, J. Pannetier, and A. W. Sleight, J. Solid State Chem. **72**, 24 (1988).
[48] J. A. Alonso, J. Amador, J. L. Martinez, I. Rasines, J. Rodriguez-Carvajal, and R. Saez-Puche, Solid State Comm. **76**, 467 (1990).
[49] X. Li *et al.*, Phys. Rev. B **89**, 064409 (2014).
[50] Y. Q. Cai *et al.*, Phys. Rev. B **93**, 014443 (2016).
[51] A. Arrott and J. E. Noakes, Phys. Rev. Lett. **19**, 786 (1967).
[52] J.-L. Jin, X.-Q. Zhang, G.-K. Li, Z.-H. Cheng, L. Zheng, and Y. Lu, Phys. Rev. B **83**, 184431 (2011).
[53] A. Midya, S. N. Das, P. Mandal, S. Pandya, and V. Ganesan, Phys. Rev. B **84**, 235127 (2011).
[54] H. Oesterreicher and F. T. Parker, J. Appl. Phys. **55**, 4334 (1984).
[55] K. A. Gschneidner Jr., V. K. Pecharsky, A. O. Pecharsky, and C. B. Zimm, Mater. Sci. Forum **315–317**, 69 (1999).
[56] J.-G. Cheng, Y. Sui, J.-S. Zhou, J. B. Goodenough, and W. H. Su, Phys. Rev. Lett. **101**, 087205 (2008).
[57] M. J. Shao, S. X. Cao, S. J. Yuan, J. Shang, B. J. Kang, B. Lu, and J. C. Zhang, Appl. Phys. Lett. **100**, 222404 (2012).
[58] C. R. H. Bahl, D. Velázquez, K. K. Nielsen, K. Engelbrecht, K. B. Andersen, R. Bulatova, and N. Pryds, Appl. Phys. Lett. **100**, 121905 (2012).
[59] N. Taira, M. Wakeshima, and Y. Hinatsu, J. Phys.: Condens. Matter **11**, 6983 (1999).
[60] K. Matsuhira, M. Wakeshima, Y. Hinatsu, and S. Takagi, J. Phys. Soc. Jpn. **80**, 094701 (2011).
[61] N. Ben Amor, M. Bejar, E. Dhahri, M. A. Valente, J. L. Garden, and E. K. Hlil, J. Alloy. Comp. **563**, 28 (2013).
[62] J. L. Wang, S. J. Campbell, J. M. Cadoan, A. J. Studer, R. Zeng, and S. X. Dou, Appl. Phys. Lett. **98**, 232509 (2011).
[63] L. W. Li, K. Nishimura, and H. Yamane, Appl. Phys. Lett. **94**, 102509 (2009).
[64] G. X. Li, J. L. Wang, Z. X. Cheng, Q. Y. Ren, C. S. Fang, and S. X. Dou, Appl. Phys. Lett. **106**, 182405 (2015).
[65] Y. M. Cao *et al.*, J. Appl. Phys. **119**, 063904 (2016).
[66] B. Li, W. J. Hu, X. G. Liu, F. Yang, W. J. Ren, X. G. Zhao, and Z. D. Zhang, Appl. Phys. Lett. **92**, 242508 (2008).
[67] L. W. Li, T. Namiki, D. X. Huo, Z. H. Qian, and K. Nishimura, Appl. Phys. Lett. **103**, 222405 (2013).
[68] J. Shen and J. F. Wu, J. Appl. Phys. **109**, 07A931 (2011).
[69] N. K. Singh, D. Paudyal, V. K. Pecharsky, and K. A. Gschneidner Jr., J. Appl. Phys. **107**, 09A921 (2010).
[70] H. Wada, Y. Tanabe, M. Shiga, H. Sugawara, and H. Sato, J. Alloy. Comp. **316**, 245 (2001).
[71] Z. J. Mo *et al.*, Appl. Phys. Lett. **103**, 052409 (2013).